ACS Catalysis

pubs.acs.org/acscatalysis
Research Article

Boosting Intramolecular Charge Transfer and Photocatalytic Hydrogen Evolution Activity of Carbon Nitride through Molecular Integration of Benzene Rings

Yingying Qin, Jian Lu, Chen Zhang, Linli Xu,* and Wai-Yeung Wong*

Cite This: ACS Catal. 2026, 16, 4440−4448
Read Online

ABSTRACT: Regulating both the in-plane structure and interlayer forces through a molecular design strategy is an effective strategy to reinforce the spatial charge separation in nonmetallic organic polymer semiconductors but remains a difficult task. Herein, we report the substitution of triazine rings with π electron-rich benzene rings to establish an intramolecular donor−acceptor (D−A)-based g-C_3N_4 (CN) polymers featuring interlayer interaction. Experimental investigations and theoretical calculations have demonstrated that the D−A structure enables fixed-point electron transfer within the plane from the donor to the acceptor segments. Additionally, the interlayer driving force arising from the internal potential difference in benzene-doped CN (BDCN) can facilitate the transfer of electrons from the B-CN layer (benzene ring-doped CN layer) to the CN sublayer. Ultrafast spectroscopy has further quantitatively confirmed that the introduction of benzene rings can greatly improve in-plane and interlayer charge separation/transfer and in turn boost the photocatalytic efficiency. Moreover, extending the π-conjugated system in BDCN can also enhance the light absorption ability. Thus, the optimized 5BDCN (252.92 μmol) exhibits a 7.3-fold increase in the photocatalytic H_2 evolution compared to pristine CN (34.48 μmol). In this study, a comprehensive understanding of the structure-performance relationship serves as a fundamental guideline for the rational design and synthesis of CN with an enhanced photocatalytic activity.

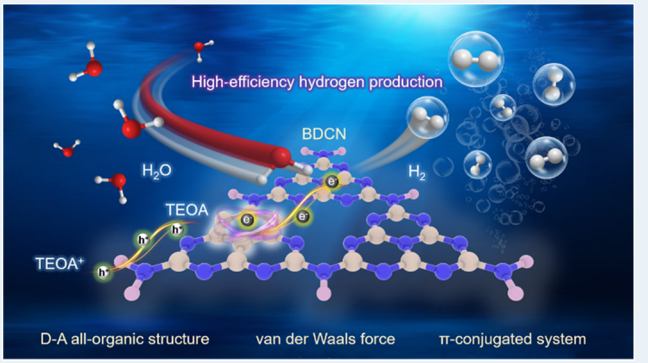

KEYWORDS: *photocatalysis, hydrogen evolution, visible-light-driven, carbon nitride, donor−acceptor, all-organic structure*

1. INTRODUCTION

With the rapid advancement of industrialization and urbanization, the ongoing consumption of fossil fuels has resulted in severe energy shortages and environmental pollution. Hydrogen energy, as an alternative energy source for fossil fuels, has been widely explored by virtue of its high energy density, cleanliness, and versatile utilization forms. Utilizing efficient and stable semiconductor photocatalysts to convert solar energy into chemical energy can meet the demands of the sustainable development globally.[1−4]

Two-dimensional (2D) materials have aroused significant attention due to their unique physicochemical properties and associated potential for commercial applications. Among various photocatalytic semiconductors, graphitic carbon nitride (g-C_3N_4, CN), featuring superior thermo/chemical stability, suitable bandgap structure, and adjustable molecular structure, is a high-profile 2D organic semiconductor material for applications in environmental remediation, pharmaceutical synthesis, and energy production.[5−7] However, its photocatalytic efficiency remains moderate due to the fact that CN usually displays undirected in-plane electron migration and weak covalence between layers, which stems from the inherent attribute of graphitic sp^2 hybridized arrangement of triazine units and the chemically inert stacking of CN multilayers.[8,9] It is primely ideal, but technically challenging, to develop a simple yet effective approach for promoting the oriented flow and separation of photogenerated electrons in the plane and interlayer of CN. As a result, multifarious research has been conducted to enhance the photocatalytic performance of CN, such as nanoengineering,[10,11] chemical doping,[12,13] heterojunction configuration,[14,15] cocatalyst loading,[15,16] and so on. Despite these efforts, the improvement in the photocatalytic performance of CN is inadequate to attain parity with those metallic photocatalysts, not to mention the requirements for large-scale applications. It is well-known that the photocatalytic activity of organic polymers is highly sensitive to the

Received: October 3, 2025
Revised: February 9, 2026
Accepted: February 10, 2026
Published: February 19, 2026

modifications of the molecular structure. Given its excellent tunability and compatibility, CN is well-suited for molecular structure design.

Enlightened by intramolecular donor−acceptor (D−A) copolymers, this approach has been extensively utilized in polymer-based solar cells. It effectively addresses the limitation of polymer charge-carrier diffusion length and enhances charge separation through intramolecular charge transfer mechanisms.[17,18] As a result, we propose the incorporation of donor or acceptor units into the CN molecular structure to form a D−A structure, which can potentially optimize the electronic properties and inherent properties of CN for elevating directional charge flow within the plane. Numerous studies authenticate the feasibility of this modification method. For example, Liu et al. showed that introducing benzo[*b*]-thiophene-2-carboxylic acid (BTH) as the donor unit into the g-C_3N_4 framework via supramolecular self-assembly to form a D−A structure could enhance the separation efficiency of photoexcited charge, resulting in the lower hydrogen molecule absorption energy and improved photocatalytic activity.[19] Che et al. prepared polymeric carbon nitride-based donor-π-acceptor (D-π-A) organic conjugated polymers by copolymerizing urea with 5-bromo-2-thiophenecarboxaldehyde, in which the photogenerated electrons in PCN-5B2T D-π-A OCPs were more easily transferred from the donor tertiary amine group to the benzene π-bridge and then to the acceptor imine group.[20] Additionally, Zhang and co-workers found that the design of an internal triazine-heptazine D−A heterostructure significantly boosted interface charge migration and achieved superior apparent quantum yields (AQYs) through a simple post-polymerization of g-C_3N_4 in NaCl/KCl eutectic salts.[21] However, these studies do not clearly elucidate how charge separation/transfer behavior between CN layers and interlayer interactions is affected when acceptor or donor monomers are grafted into CN molecules. Therefore, it is particularly important to investigate the relationship between interlayer interactions and charge transport behavior at the molecular level.

Herein, we successfully built a D−A all-organic structure by seamlessly inosculating a benzene ring as the donor unit into the CN skeleton, forming sp^2-hybridized C−N bonds through a simple thermal polycondensation method. This approach allowed us to explore the potential energy difference between the benzene ring-modified CN layer (B-CN) and the adjacent CN sublayer. The D−A structure with interlayer interaction can promote spatial charge separation and enhance the light absorption intensity through theoretical and experimental verification. Consequently, 5BDCN has excellent control over the comprehensive charge flow and exhibits superior photocatalytic H_2 evolution activity under visible-light exposure.

2. MATERIALS AND METHODS

2.1. Materials

Melamine, 1,3,5-triaminobenzene (TAB), and chloroplatinic acid ($H_2PtCl_6{\cdot}6H_2O$) were provided by Aladdin Reagent Company, China. Ethanol (C_2H_5OH, 95.0%) and triethanolamine (TEOA) were purchased from Sinopharm Chemical Reagent Co., Ltd. Deionized water was used throughout this study. The reagents are all of analytical grade without further purification.

2.2. Synthesis Method of Catalysts

Benzene-doped g-C_3N_4 (BDCN) was prepared through thermal polycondensation. In this process, melamine serves as the precursor, and 1,3,5-triaminobenzene is used as the monomer unit for doping benzene moieties, replacing triazine aromatic rings in the planar network of g-C_3N_4 (Scheme 1). The resulting dark yellow polymer

Scheme 1. Illustration of the Chemical Reaction for the Preparation of BDCN

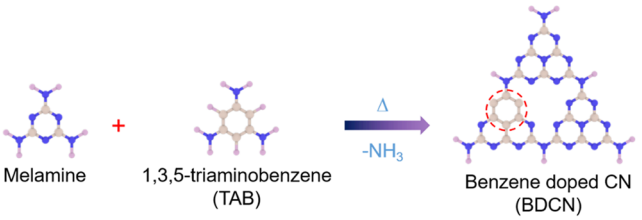

sample is designated as XBDCN, where "*X*" indicates the amount of 1,3,5-triaminobenzene added, in mg. The detailed procedure is as follows: First, different amounts of 1,3,5-triaminobenzene (5 and 10 mg) and 10 g of melamine were placed in an agate mortar and ground together for 30 min to achieve a uniform mixture. Then, the mixture was transferred to an alumina crucible with a cover and heated in a muffle furnace under an air atmosphere at a heating rate of 3 °C min^{-1} from room temperature to 550 °C, where it was maintained for 5 h. In this study, we optimized 5BDCN as the photocatalyst. The chemical reaction in the process is illustrated in Scheme 1.

2.3. Activity Measurement

The photocatalytic hydrogen production activity of the reconstructed materials was tested using the hydrogen evolution process under irradiation from a 300 W xenon lamp ($\lambda \geq 420$ nm, Prefectlight, PLS-SXE300C). First, 50 mg of the photocatalyst powder was added to 100 mL of an aqueous solution containing 20 vol % TEOA as the hole scavengers. Then, a certain amount of $H_2PtCl_6{\cdot}6H_2O$ (Pt, 3 wt %) was added to the mixture as a cocatalyst and loaded onto the surface of the photocatalysts via light irradiation. The reaction solution was then repeatedly aspirated to completely eliminate air. The reaction temperature was kept at 10 °C by using an external circulating cooling water system. The gases generated by the photocatalytic reaction were analyzed using an online gas chromatograph equipped with a thermal conductivity detector (TCD).

The apparent quantum efficiency (AQE) was measured under the same conditions used for the photocatalytic hydrogen evolution experiments. A Xe lamp served as the light source equipped with different band-pass filters (λ = 400, 420, 450, 500, and 600 nm). The AQE was calculated by using the following equation

$$\mathrm{AQE}\ (\%) = \frac{2 \times \text{number of formed } H_2 \text{ molecules}}{\text{number of incident photons}} \times 100\%$$

2.4. Catalyst Characterizations

For detailed catalyst characterizations, please refer to the Supporting Information.

3. RESULTS AND DISCUSSION

3.1. Characterization of Photocatalysts

The crystalline structure characteristics of the as-synthesized materials were investigated by using X-ray diffraction (XRD). As depicted in Figure 1a, the plain CN shows two main characteristic diffraction peaks at 13.1° and 27.5°, which correspond to the (100) plane, stemming from the in-plane packing structure of conjugated tri-s-triazine, and the (002) plane associated with the interlayer stacking of the conjugated aromatic segments, respectively.[22] Compared to CN, the (002) diffraction peak of 10BDCN shifts toward a lower angle, suggesting that the substitution of triazine rings in CN with benzene rings could increase the stacking distance (Figure 1b).[23] This phenomenon may be attributed to the incorpo-

https://doi.org/10.1021/acscatal.5c06958
ACS Catal. 2026, 16, 4440−4448

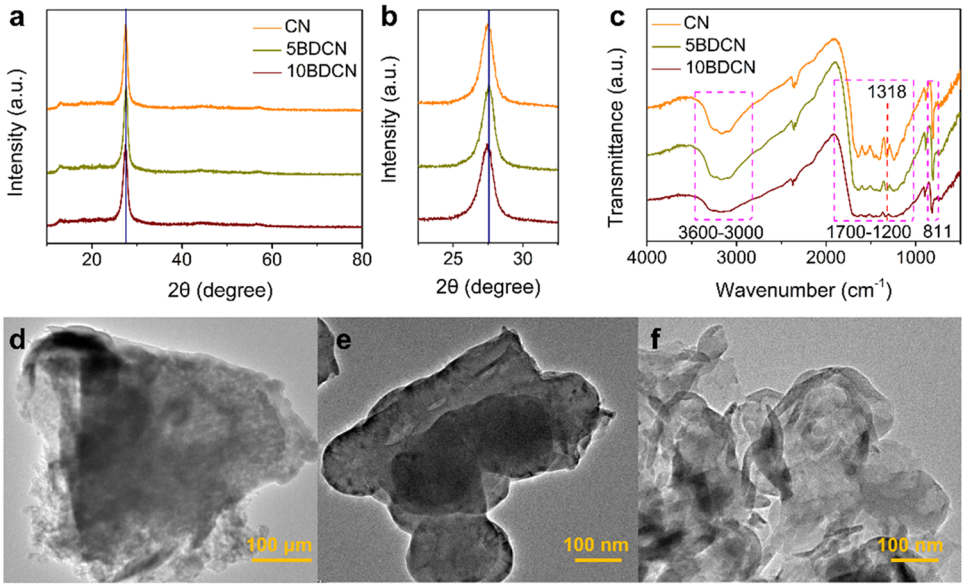

Figure 1. (a) XRD patterns, (b) the enlarged XRD patterns, and (c) FTIR spectra of CN, 5BDCN, and 10BDCN. TEM images of (d) CN, (e) 5BDCN, and (f) 10BDCN.

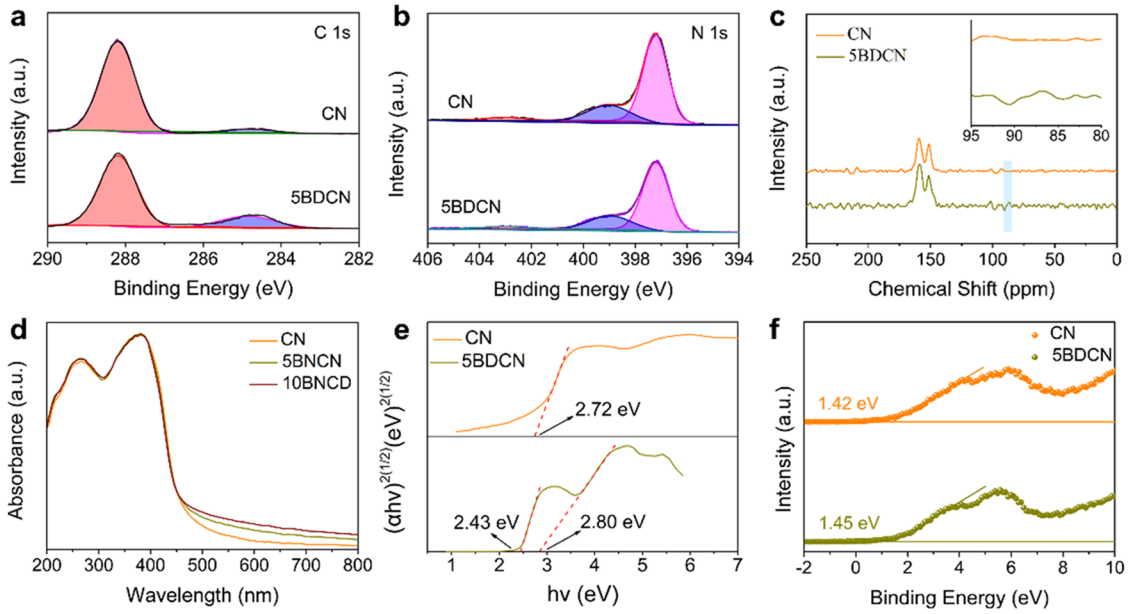

Figure 2. XPS spectra of pure CN and 5BDCN: (a) C 1s and (b) N 1s. (c) Solid-state ^{13}C NMR spectra of CN and 5BDCN. The inset of (c) shows the magnified spectra of the blue region. (d) UV−Vis spectra of CN, 5BDCN, and 10BDCN. (e) The plots of $(ahv)^{1/2}$ versus (hv), and (f) XPS valence band spectra of CN and 5BDCN.

ration of benzene rings, which enhance interlayer interactions and modifies the stacking mode between layers, thereby leading to changes in the interlayer spacing. The unchanged (002) characteristic peak of 5BDCN might be due to the small amount of TBA added, making it nearly undetectable. The chemical composition and microstructure of CN, 5BDCN, and 10BDCN samples were further analyzed using Fourier transform infrared (FTIR) spectra (Figure 1c). Notably, all samples exhibit similar characteristic peaks, manifesting that the core chemical configuration of g-C_3N_4 remains unchanged after the introduction of benzene rings. The typical sharp peak at around 811 cm^{-1} is attributed to the out-of-plane bending characteristic of tri-s-triazine units. A series of absorption peaks between 1200 and 1700 cm^{-1} correspond to the stretching modes of aromatic carbon−nitrogen heterocycles, while the broad absorption peak in the range of 3000 to 3600 cm^{-1} is related to the stretching vibrations of N−H and O−H, stemming from uncondensed amine groups and physically absorbed water. In addition, the stretching vibration peak at approximately 1318 cm^{-1} in 10BDCN moves slightly to the higher frequency region, which is attributed to the introduction of 1,3,5-triaminobenzene monomers to reduce the number of N atoms with high electronegativity in CN, thereby reinforcing the strength of adjacent C−N covalent bonds in the heptazine skeleton.[24] The above results preliminarily confirm the presence of benzene rings in the CN molecular structure.

To further observe the microstructural differences and nanosheet thickness of the resultant products in detail,

https://doi.org/10.1021/acscatal.5c06958
ACS Catal. 2026, 16, 4440−4448

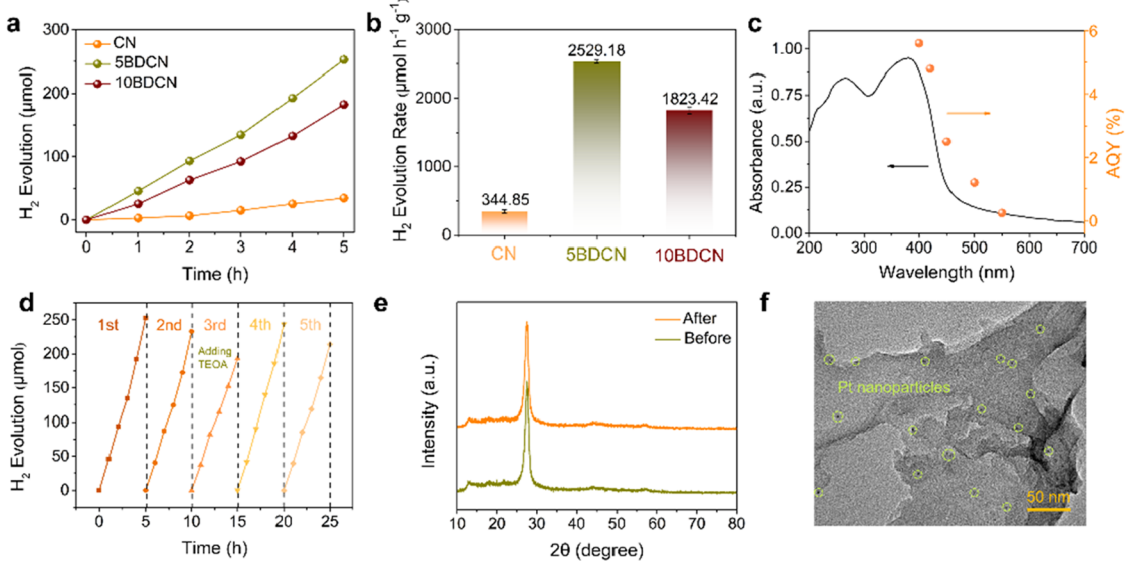

Figure 3. (a) Time courses of photocatalytic H_2 evolution of the as-prepared samples and (b) photocatalytic H_2 evolution rates of CN, 5BDCN, and 10BDCN under visible-light irradiation. (c) Wavelength-dependent AQE of H_2 evolution over 5BDCN. (d) Stability study of photocatalytic H_2 evolution by 5BDCN. (e) PXRD patterns and (f) TEM image of 5BDCN after five catalytic cycles.

transmission electron microscopy (TEM) and atomic force microscopy (AFM) analyses were conducted. The morphology of bulk CN obtained through traditional thermal polymerization is consistent with the previous reports.[25,26] The TEM image of bulk CN (Figure 1d) clearly shows a 2D irregular nanosheet stacking structure with a size of several micrometers. By addition of 5 mg of 1,3,5-triaminobenzene to melamine for calcination, the appearance of 5BDCN changes. As observed from Figure 1e, the edges of the 5BDCN nanosheets gradually become clear, and the stacking of nanosheets is reduced, showing a smooth and flat surface. When the amount of 1,3,5-triaminobenzene added to melamine is increased to 10 mg, 10BDCN exhibits a 2D lamellar structure with folded edges (Figure 1f). The AFM images of the as-prepared samples (Figure S1) provide detailed insights into the morphological changes. By comparison, it can be observed that the appropriate addition of 1,3,5-triaminobenzene effectively suppresses the stacking of nanosheets during the thermal polymerization of melamine.

To investigate the effect of benzene ring insertion on the chemical compositions and elemental states of the samples, X-ray photoelectron spectroscopy (XPS) and solid-state ^{13}C NMR spectra were obtained. As shown in Figure S2, the survey spectra of CN and 5BDCN reveal the existence of C, N, and O elements. The presence of O is likely due to the adsorption of H_2O and CO_2 molecules on the sample surface. In Figure 2a, the C 1s XPS spectra of CN and 5BDCN can be deconvoluted into two peaks, corresponding to aromatic carbon atoms at 284.8 eV (C/C═C) and sp^2-hybridized carbon atoms at 286.7 eV (N−C═N/C−N═C). It is worth noting that the peak intensity at 283.3 eV for 5BDCN is significantly higher than that for CN, indicating the successful introduction of benzene rings into the molecular structure of CN.[27] Moreover, the high-resolution N 1s spectrum of 5BDCN can be divided into the terminal amino nitrogen (C−NH) at 403.1 eV, the tertiary nitrogen (N−$(C)_3$) at 398.9 eV, and the sp^2-hybridized aromatic nitrogen atom at 397.2 eV (N−C═N/C−N═C) (Figure 2b). Similarly, the N−$(C)_3$ peak for 5BDCN is stronger than that for pure CN, indicating that the terminal amino group on the CN skeleton has been replaced by aromatic benzene carbon.[28] These changes in the intensities of the C 1s and N 1s peaks are attributed to the redistribution of electrons resulting from the incorporation of benzene rings with a rich π-electron structure into the CN framework. In addition, solid-state ^{13}C NMR spectra further provided additional confirmation that the triazine ring in CN has been substituted by the benzene ring. Compared with CN, 5BDCN shows a new characteristic peak at 86.7 ppm, which may come from the aromatic carbon (Figure 2c).[29] The analytical results presented above corroborate that benzene rings are introduced into the CN molecule during the pyrolysis process.

The UV−Vis spectra of the CN series reflect their electronic structures and optical properties. As displayed in Figure 2d, both CN and XBDCN present typical semiconductor absorption across a wide wavelength range from UV to visible light. The modification of CN with benzene rings has no effect on the position of the absorption edge, which remains around 470 nm for all materials. Additionally, the absorption intensity of 5BDCN significantly increases in the wavelength range of 500−800 nm, which is probably due to the enhanced D−A interactions and ordered $\pi-\pi$ stacking in 5BDCN.[30] Thus, incorporating benzene rings into the CN molecular structure can effectively improve its electronic structure and photoresponse capability. Based on the transformational Taus plots, the calculated band gaps (E_g) of CN and 5BDCN are estimated to be 2.72 and 2.80 eV, respectively (Figure 2e). The introduction of benzene rings generates midgap states (E_m) located at 2.43 eV above the valence band (VB) position, thereby adjusting the energy band configuration of CN. The midgap states can receive electrons from the VB of 5BDCN, which is beneficial to absorb photons with energy lower than the bandgap.[31] XPS-VB results indicate that the VB energies of CN and 5BDCN are 1.42 and 1.45 eV, respectively (Figure 2f). In light of the above experimental analysis, the energy band structures of CN and 5BDCN are schematically illustrated in Figure S3. The conduction band (CB) upshift in 5BDCN makes the thermodynamic driving force stronger,

https://doi.org/10.1021/acscatal.5c06958
ACS Catal. 2026, 16, 4440−4448

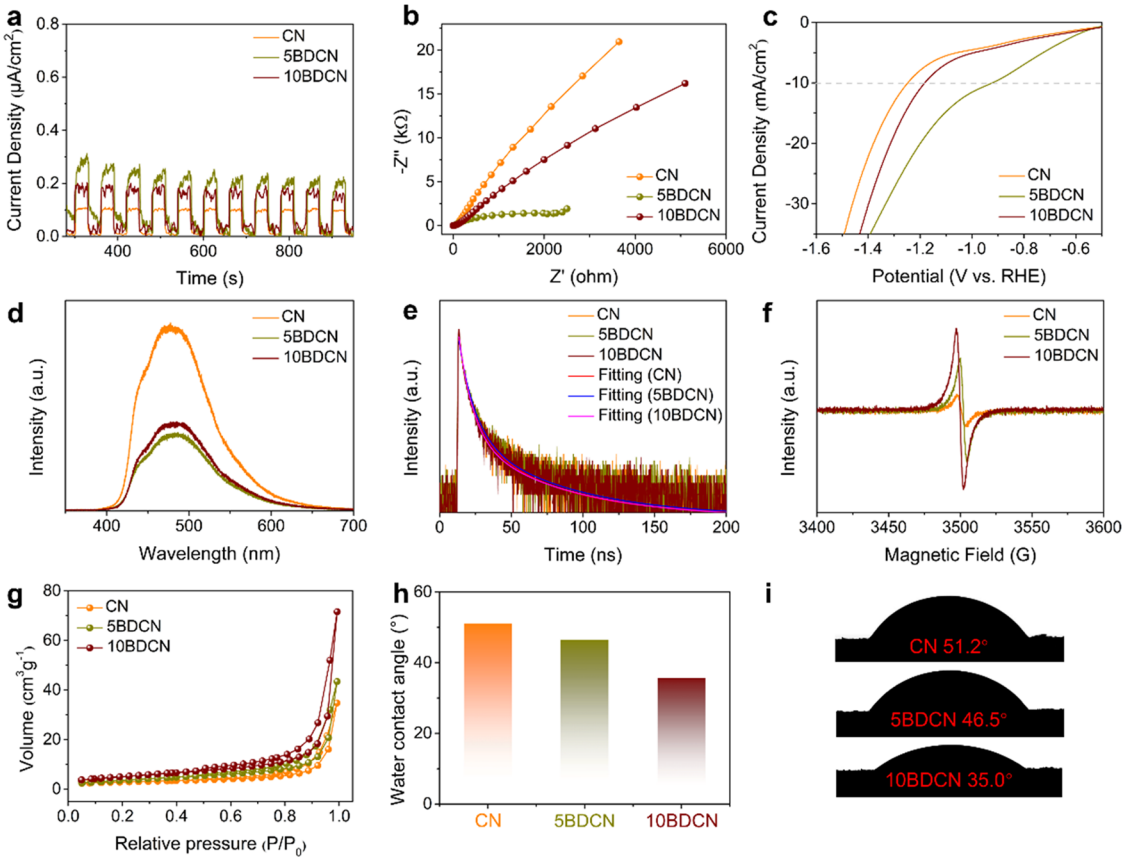

Figure 4. (a) Transient photocurrent response, (b) Nyquist plots derived from EIS measurements, (c) polarization curves, (d) PL spectra, (e) time-resolved fluorescence decay spectra, (f) EPR spectra, (g) nitrogen adsorption/desorption isotherms, (h) water contact angle measurements, and (i) water contact angle photos of CN, 5BDCN, and 10BDCN.

generating more electrons and holes, thereby enhancing the photocatalytic H_2 evolution performance.

3.2. Photocatalytic Hydrogen Evolution Performance

The photocatalytic H_2 evolution experiments for the modified CN with a Pt cocatalyst were conducted under light irradiation (AM 1.5) in water with TEOA as the sacrificial reagent. Gas chromatography with a thermal conductivity detector was used to monitor the H_2 production yield per hour during a 5 h period. The pristine CN has a relatively low photocatalytic H_2 evolution activity of 34.48 μmol due to the rapid recombination of electrons and holes. When 5 mg of 1,3,5-triaminobenzene was added, the photocatalytic activity for H_2 evolution reached up to 252.92 μmol, representing an approximately 7.3-fold improvement compared to that of the pristine CN. The H_2 evolution amount for 10BDCN was 182.34 μmol (Figure 3a). Excessive addition of 1,3,5-triaminobenzene generated more defects, leading to charge recombination. In addition, the H_2 liberation rates of CN, 5BDCN, and 10BDCN were 346.46, 2529.18, and 1823.42 μmol h^{-1} g^{-1}, respectively (Figure 3b). These experimental results clearly indicate that the photocatalytic H_2 evolution is influenced by the doping content of the benzene rings. The D−A structure formed by introducing an appropriate amount of benzene rings into the CN molecular framework promotes the ordered transport of charge carriers within the B-CN plane. Furthermore, the driving force between the B-CN and the adjacent CN layers can further facilitate the spatial separation and transport of charge carriers, improving electron utilization efficiency. As shown in Figure S4, the photocatalytic hydrogen evolution performance is significantly reduced or even nearly absent when the system lacks the photocatalyst, TEOA, light irradiation, or the cocatalyst. These results demonstrate the necessity of all these components for the efficient operation of the 5BDCN catalytic system. Doping with benzene rings also narrows the bandgap of CN and extends the visible-light response range. The optical absorption spectrum of 5BDCN shows a trend similar to the variation in apparent quantum efficiency (AQE), illustrating that the photoexcitation of 5BDCN facilitates H_2 formation (Figure 3c). The photocatalytic H_2 evolution activity of 5BDCN was stable over consecutive cycle tests (25 h), with appropriate supplementation of TEOA as needed (Figure 3d). After five cycles, the PXRD pattern and TEM images of the collected 5BDCN revealed that the characteristic peaks were well preserved, confirming its satisfactory stability (Figure 3e,f).

3.3. Photoelectrochemical (PEC) Properties and Charge Transfer Dynamics

Based on the photocatalytic H_2 evolution results, it can intuitively demonstrate that the synergistic effect of the in-plane D−A structure and internal interaction force can considerably improve the photocatalytic performance and stability, which is ascribed to the effective spatial charge separation. To further validate this hypothesis, the PEC measurements were implemented to explore the charge separation characters. The transient photocurrent responses are listed in Figure 4a. In stark contrast, the pure CN sample has the weakest photoresponse (ca. 0.10 μA cm^{-2}), while the saturated photocurrent density of 5BDCN (ca. 0.54 μA cm^{-2})

https://doi.org/10.1021/acscatal.5c06958
ACS Catal. 2026, 16, 4440−4448

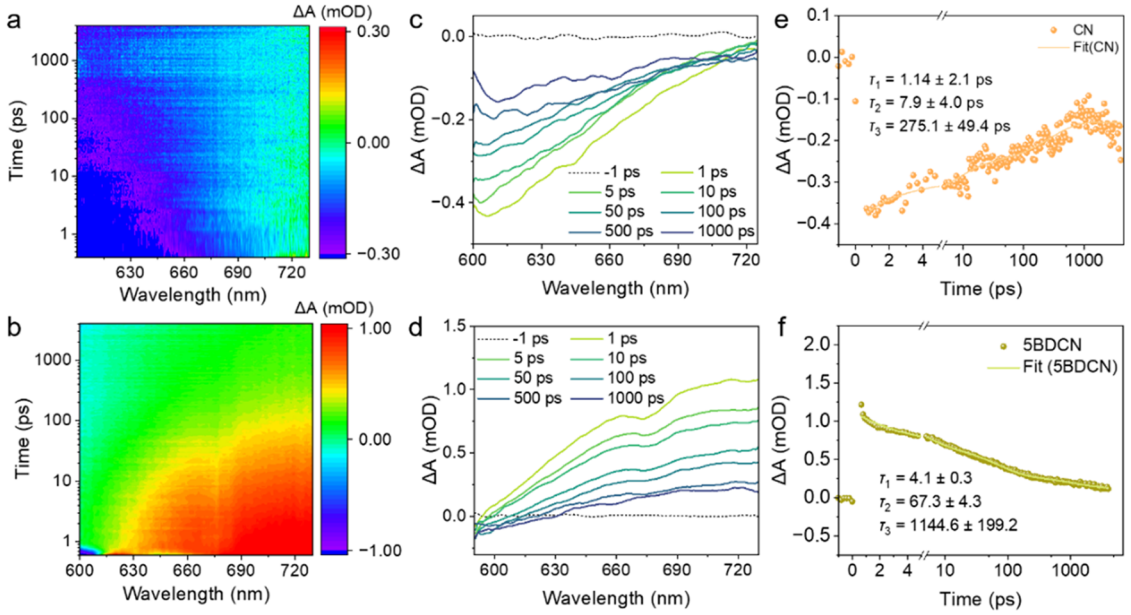

Figure 5. 2D pseudocolor maps of (a, b) fs-TA spectra and (c, d) transient fs-TA spectra at various probe delays for CN and 5BDCN. Kinetics probed at 700 nm for (e) CN and (f) 5BDCN. The inset summarizes the corresponding parameters.

is nearly three times higher than that of 10BDCN (ca. 0.18 μA cm^{-2}) upon switching the irradiation on (or off), thus implying that the introduction of an appropriate amount of 1,3,5-triaminobenzene can significantly promote the charge separation. The electrochemical impedance spectra (EIS) of CN, 5BDCN, and 10BDCN are depicted in Figure 4b. The charge transfer resistance (R_{ct}) is proportional to the arc of the semicircle, representing the difficulty of charge exchange between the photocatalyst and reactants in the electrolyte.[32] Obviously, the BDCN composites show smaller R_{ct} values compared to CN under the same experimental conditions, suggesting that the interfacial electron-transfer resistance in BDCN is much smaller than CN, so the D−A structure and interlayer interaction force greatly improve the in-plane and interlayer charge separation and transfer. In the range of −0.5 to −1.6 V (vs Ag/AgCl), the order of cathode current density is 5BDCN > 10BDCN > CN, which aligns well with the photocatalytic activity of the as-prepared samples (Figure 4c). As shown in Figure 4d, all samples exhibit a main peak at approximately 470 nm. The quenched steady-state photoluminescence (PL) intensity of 5BDCN represents superior separation and transfer of photoexcited charge carriers.[33] Besides, time-resolved photoluminescence (TR-PL) spectra were used to quantitatively analyze the charge-carrier lifetimes of the resultant products via a biexponential fitting equation $I(t) = A_1 \times \exp\left(\frac{-t}{\tau_1}\right) + A_2 \times \exp\left(\frac{-t}{\tau_2}\right)$. The average lifespan was calculated by $\tau_{ave} = \frac{(A_1\tau_1 + A_2\tau_2)}{(A_1 + A_2)}$. As shown in Table S2, the average charge lifetime of 5BDCN is 38.41 ns, which is nearly 7% longer than that of CN with 35.75 ns fluorescent lifetime. This reveals that the modification method of CN is effective in triggering charge separation and transfer (Figure 4e). The electron paramagnetic resonance (ESR) spectra are shown in Figure 4f, and all samples present a Lorentz line at g = 2.0035, which is attributed to the presence of unpaired π electrons on sp^2 carbon atoms within the aromatic rings. Compared to CN, the ESR intensity of 5BDCN and 10BDCN increases significantly, indicating that the defect concentration within the molecule is positively correlated with the amount of 1, 3, 5-triaminobenzene added, and a higher concentration of unpaired electrons is produced. These highly reactive unpaired electrons can combine with protons to generate hydrogen, thereby effectively enhancing the photocatalytic performance.[33,34] It is also found that the g value of BDCN shifts slightly, indicating that the π-conjugated system within the BDCN molecule is expanded, thereby effectively improving the charge migration efficiency. In addition, the specific surface area and hydrophilicity of the material also affect the photocatalytic performance. The test results show that all samples have a type-IV reversible isotherm, indicative of their mesoporous structures. The BET surface areas of CN, 5BDCN, and 10BDCN are calculated to be 9.63, 13.0, and 18.63 m^2 g^{-1}, respectively (Figure 4g), in which the larger surface area offers abundant active sites for photocatalytic reaction, and the porous structure can expedite the kinetics of mass (i.e., reactant and product). 5BDCN also shows a good hydrophilic property, allowing it to adsorb a large number of water molecules for HER in an aqueous environment (Figure 4h,i).

To further explore the influence of benzene ring incorporation on charge transfer and separation in 5BDCN, femtosecond transient absorption (fs-TA) measurements were conducted by using a 450 nm pump pulse. Figure 5 displays the 2D pseudocolor maps of CN and 5BDCN (Figure 5a, d) and their corresponding fs-TA spectra at various delay times (−1 to 1000 ps, as shown in Figure 5b,e). Upon light excitation, pristine CN presents only a broad, negative absorption band in the range of 590 to 690 nm, corresponding to overlapping ground state bleaching (GSB) and stimulated emission (SE) signals.[35,36] Different from CN, 5BDCN also has a positive TAS signal at 610−730 nm, in addition to the negative TAS signal. These positive signals are primarily due to the excited-state absorption (ESA) of photoinduced electrons,[37] corroborating that the D−A structure can allow the electron fixed-point transfer within the plane and generate a

https://doi.org/10.1021/acscatal.5c06958
ACS Catal. 2026, 16, 4440−4448

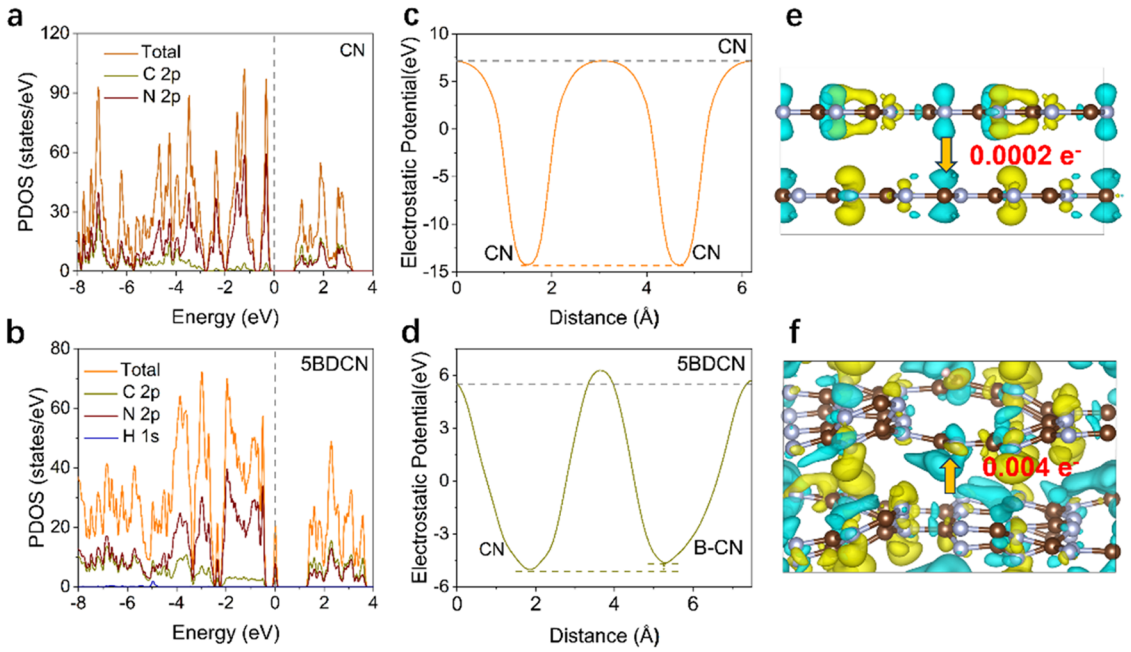

Figure 6. Local density of states for (a) CN and (b) 5BDCN. Layered electrostatic potential energy for pristine (c) CN and (d) 5BDCN. Charge density difference for (e) CN and (f) 5BDCN (cyan and yellow areas represent electron accumulation and depletion, respectively).

potential energy difference between the B-CN layer and the CN sublayer, thereby accelerating the charge transfer. The decay kinetics of the samples at 700 nm were fitted using a three-exponential model (Figure 5e,f). The short lifetime (several picoseconds) of τ_1 is mainly attributed to electron diffusion. The other two slower quenching processes belong to the electron recombination in the conduction band minimum (CBM) with holes in the valence band maximum (VBM) and the trapped state, respectively. Since the hole-trapping state is higher than the VBM, the second electron decay pathway (τ_2 = 67.3 ± 4.3 ps) is accredited to electron recombination with the trapped holes. The slowest electron decay pathway, with a prolonged lifetime (τ_3 = 1144.6 ± 199.2 ps), is attributed to the recombination of charge carriers. The 5BDCN shows a prolonged decay lifetime τ_3 than that of the pristine CN (τ_3 = 275.1 ± 49.4 ps), indicating that the charge recombination is effectively suppressed, providing more electrons to participate in the photocatalytic HER. The test results further validate the positive role of the introduction of a benzene ring.

Density functional theory (DFT) calculations were conducted to analyze the influence of benzene ring doping on the electronic structure of CN. In light of the local density of states (DOS, Figure 6a,b), the CB and VB of CN and 5BDCN are mainly composed of N 2p orbitals and C 2p orbitals. Comparative analysis of the density of states reveals that benzene doping introduces new impurity levels near the Fermi energy of 5BDCN, indicating a significant enhancement in its electron transport capability.[38] Due to the well-known limitation of the generalized gradient approximation (GGA) functional (low exchange correlation between electrons), the calculated bandgap is markedly smaller than the experimental value. The bandgap of 5BDCN is narrower than that of CN, ameliorating its visible-light absorption ability.[39] The calculation result aligns well with the DRS analysis, signifying that the electrons in 5BDCN are more readily excited. Comparative analysis of the work function (Figure 6c,d) reveals that the vacuum energy levels on both sides of the CN structure are highly consistent, indicating that the built-in electric field at the interface can be neglected. However, after benzene doping, the vacuum energy level on the B-CN side increases significantly and the local work function becomes larger. This creates a potential gradient between the CN and B-CN layers, facilitating electron migration toward the B-CN side and resulting in a certain degree of interlayer charge separation. Furthermore, the differential charge density maps reveal that there is almost no electron transfer between the layers of CN without benzene ring doping, with the charge primarily localized within each individual layer (as shown in Figure 6e). In contrast, the interlayer charge transfer in 5BDCN is significantly enhanced, which can be mainly attributed to the effective strengthening of the interlayer interactions, thereby facilitating charge transport between the layers.

3.4. Mechanism Discussion

Based on the above analysis, a photocatalytic HER mechanism in the 5BDCN photocatalytic system is proposed. Compared to pure CN, 5BDCN has the following advantages: (i) Intramolecular D−A all-organic structure. The replacement of some triazine rings with a π-electron-rich benzene ring makes the B-CN plane to bend. Electrons concentrated around the triazine rings are primarily derived from the benzene ring, facilitating quick and directional electron transfer. (ii) Interlayer interaction force. The intermolecular interlayer interaction force acts as a driving force, pushing electrons from the B-CN layer to the CN sublayer. This is due to the significant potential energy difference between the B-CN layer and the CN sublayer within 5BDCN, which aids in the spatial charge separation and transfer. (iii) π-conjugated system. The high degree of π-conjugation in 5BDCN can improve the visible-light absorption. Under light irradiation, the electrons in the VB are excited to the CB, leaving the holes in the VB. The D−A structure and interlayer interaction force can restrain the recombination of electrons and holes. Electrons in the CB are readily captured and stored by Pt cocatalysts, which have a low overpotential for H_2 reduction for improving the photo-

https://doi.org/10.1021/acscatal.5c06958
ACS Catal. 2026, 16, 4440−4448

catalytic activity of 5BDCN, where the electrons combine with protons to release H_2. In addition, the holes are oxidized by TEOA, further enhancing the photocatalytic performance. This proposed mechanism highlights the synergistic effects of the D−A structure, interlayer interaction force, and π-conjugated system in improving the photocatalytic efficiency of 5BDCN.

4. CONCLUSIONS

In summary, we have successfully built a D−A all-organic structure to facilitate vectorial electron transfer and optimize the photocatalytic H_2 evolution activity by the introduction of benzene ring units into the basal plane of g-C_3N_4 through a simple thermal polycondensation method. Owing to the efficient intramolecular charge transfer within the D−A system and internal interaction force, 5BDCN presents an enhanced electron−hole separation ability, resulting in a remarkable photocatalytic performance. Moreover, incorporating benzene rings into CN improves the light absorption intensity. Therefore, this approach provides an internal driving force for interlayer and in-plane charge transfer, efficiently directing photoinduced electrons to the active reaction sites.

■ ASSOCIATED CONTENT

Supporting Information

The Supporting Information is available free of charge at https://pubs.acs.org/doi/10.1021/acscatal.5c06958.

Details of catalyst characterizations; results of AFM and XPS survey; band structure diagram; results of control experiments; performance comparison; and lifetime fitting results (PDF)

■ AUTHOR INFORMATION

Corresponding Authors

Linli Xu − *Department of Applied Biology and Chemical Technology and Research Institute for Smart Energy, The Hong Kong Polytechnic University, Kowloon, Hong Kong 999077, P. R. China;* orcid.org/0000-0002-7032-9464; Email: linli.xu@polyu.edu.hk

Wai-Yeung Wong − *Department of Applied Biology and Chemical Technology and Research Institute for Smart Energy, The Hong Kong Polytechnic University, Kowloon, Hong Kong 999077, P. R. China;* orcid.org/0000-0002-9949-7525; Email: wai-yeung.wong@polyu.edu.hk

Authors

Yingying Qin − *Department of Applied Biology and Chemical Technology and Research Institute for Smart Energy, The Hong Kong Polytechnic University, Kowloon, Hong Kong 999077, P. R. China; School of Chemistry and Chemical Engineering, Hainan University, Haikou 570228, P. R. China*

Jian Lu − *School of Chemistry and Chemical Engineering, Hainan University, Haikou 570228, P. R. China*

Chen Zhang − *Department of Applied Biology and Chemical Technology and Research Institute for Smart Energy, The Hong Kong Polytechnic University, Kowloon, Hong Kong 999077, P. R. China*

Complete contact information is available at: https://pubs.acs.org/10.1021/acscatal.5c06958

Notes

The authors declare no competing financial interest.

■ ACKNOWLEDGMENTS

W.-Y.W. thanks the financial support from the RGC Senior Research Fellowship Scheme (SRFS2021-5S01), the Hong Kong Research Grants Council (PolyU 15307321 and C5081-21E), the Research Institute for Smart Energy (CDAQ), the Research Centre for Nanoscience and Nanotechnology (CE2H), the Research Centre for Carbon-Strategic Catalysis (CE41), and Miss Clarea Au for the Endowed Professorship in Energy (847S). L.L.X. is grateful for the financial support from the Hong Kong Research Grants Council (PolyU 25301524) and the Hong Kong Polytechnic University (1-WZ0Z, 1-BEBA, 1-CE2N, RCNN). J.L. thanks the National Natural Science Foundation of China (No. 22308126). The authors would like to thank Tong Qi (from Scientific Compass www.shiyanjia.com) for the ^{13}C NMR analysis.

■ REFERENCES

(1) He, T.; Zhen, W.; Chen, Y.; Guo, Y.; Li, Z.; Huang, N.; Li, Z.; Liu, R.; Liu, Y.; Lian, X.; Xue, C.; Sum, T.; Chen, W.; Jiang, D. Integrated Interfacial Design of Covalent Organic Framework Photocatalysts to Promote Hydrogen Evolution from Water. *Nat. Commun.* **2023**, *14*, No. 329, DOI: 10.1038/s41467-023-35999-y.

(2) Li, C.; Guo, R.; Yi, W.; Wang, S.; Du, X.; Liu, Y.; Liu, Z.; Chen, J.; Yue, X. Visible-Light-Driven Inactivation of Bacteria and H_2 Generation Catalyzed by Oxygen-Vacancy-Rich One-Dimensional/Two-Dimensional $W_{18}O_{49}$/g-C_3N_4 Z-Scheme Heterostructures. *ACS Appl. Mater. Interfaces* **2024**, *16* (14), 17432−17441.

(3) Chang, C.; Lin, W.; Ting, L.; Shih, C.; Chen, S.; Huang, T.; Tateno, H.; Jayakumar, J.; Jao, W.; Tai, C.; Chu, C.; Chen, C.; Yu, C.; Lu, Y.; Hu, C.; Elewa, A. M.; Mochizuki, T.; Chou, H. Main-Chain Engineering of Polymer Photocatalysts with Hydrophilic Non-conjugated Segments for Visible-Light-Driven Hydrogen Evolution. *Nat. Commun.* **2022**, *13*, No. 5460.

(4) Jiang, T.; Wang, Z.; Wei, G.; Wu, S.; Huang, L.; Li, D.; Ruan, X.; Liu, Y.; Jiang, C.; Ren, F. Defective High-Crystallinity g-C_3N_4 Heterostructures by Double-End Modulation for Photocatalysis. *ACS Energy Lett.* **2024**, *9* (4), 1915−1922.

(5) Zhang, X.; Su, H.; Cui, P.; Cao, Y.; Teng, Z.; Zhang, Q.; Wang, Y.; Feng, Y.; Feng, R.; Hou, J.; Zhou, X.; Ma, P.; Hu, H.; Wang, K.; Wang, C.; Gan, L.; Zhao, Y.; Liu, Q.; Zhang, T.; Zheng, K. Developing Ni Single-Atom Sites in Carbon Nitride for Efficient Photocatalytic H_2O_2 Production. *Nat. Commun.* **2023**, *14*, No. 7115.

(6) Tomita, Y.; Taira, N.; Sakai, K.; Ozawa, H. Efficient Visible-Light-Driven Water Oxidation by a Carbon Nitride Modified with Cobalt Polyoxometalate Molecular Catalyst. *ACS Catal.* **2024**, *14* (8), 5788−5794.

(7) Sun, Z.; Lu, Y.; Zhu, L.; Liu, W.; Ou, Y.; Lin, N.; Yu, P. Simultaneous Separation, Concentration and Determination of Trace Fluoroquinolone Antibiotics in Environmental Samples using a Polymer Aqueous Two-Phase System Coupled with HPLC. *J. Chem. Technol. Biotechnol.* **2019**, *94* (9), 2917−2927.

(8) Cui, W.; Li, J.; Cen, W.; Sun, Y.; Lee, S. C.; Dong, F. Steering the Interlayer Energy Barrier and Charge Flow via Bioriented Transportation Channels in g-C_3N_4: Enhanced Photocatalysis and Reaction Mechanism. *J. Catal.* **2017**, *352*, 351−360.

(9) Wang, L.; Cheng, W.; Wang, J.; Yang, J.; Liu, Q. Construction of Intramolecular and Interfacial Built-in Electric Field in a Donor-Acceptor Conjugated Polymers-Based S-Scheme Heterojunction for High Photocatalytic H_2 Generation. *Chin. J. Catal.* **2024**, *58*, 194−205.

(10) Jiang, D.; Hu, S.; Qu, Y.; Tian, X.; Du, H.; Zhu, C.; Li, Z.; Yin, L.; Yuan, Y.; Liu, G. Infrared Irradiation-Lattice Vibration Coupling-Initiated N → π^* Electronic Transition in Carbon Nitride Nanosheets for Increased Photocatalysis. *Adv. Funct. Mater.* **2024**, *34* (16), No. 2311803.

(11) Qin, Y.; Lu, J.; Zhao, X.; Lin, X.; Hao, Y.; Huo, P.; Meng, M.; Yan, Y. Nitrogen Defect Engineering and π-Conjugation Structure

Decorated g-C_3N_4 with Highly Enhanced Visible-Light Photocatalytic Hydrogen Evolution and Mechanism Insight. *Chem. Eng. J.* **2021**, *425*, No. 131844.
(12) Wang, H.; Jiang, J.; Yu, L.; Peng, J.; Song, Z.; Xiong, Z.; Li, N.; Xiang, K.; Zou, J.; Hsu, J.-P.; Zhai, T. Tailoring Advanced N-Defective and S-Doped g-C_3N_4 for Photocatalytic H_2 Evolution. *Small* **2023**, *19*, No. 2301116.
(13) Liu, Q.; Kang, S.; Cui, Z.; Liu, Y.; Zhang, M.; Zhang, Z. Visible Light-Driven C-H Arylation of Heteroarenes with Aryl Diazonium Salts in Water Catalyzed by a Z-Scheme $CuInS_2$/K-C_3N_4 Heterojunction. *Green Chem.* **2024**, *26*, 4803−4810.
(14) Qin, Y.; Li, H.; Lu, J.; Feng, Y.; Meng, F.; Ma, C.; Yan, Y.; Meng, M. Synergy between Van Der Waals Heterojunction and Vacancy in $ZnIn_2S4$/g-C_3N_4 2D/2D Photocatalysts for Enhanced Photocatalytic Hydrogen Evolution. *Appl. Catal., B* **2020**, *277*, No. 19254.
(15) Liu, D.; Jiang, L.; Chen, D.; Hao, Z.; Deng, B.; Sun, Y.; Liu, X.; Jia, B.; Chen, L.; Liu, H. Twin S-Scheme g-C_3N_4/$CuFe_2O_4$/$ZnIn_2S_4$ Heterojunction with a Self-Supporting Three-Phase System for Photocatalytic CO_2 Reduction: Mechanism Insight and DFT Calculations. *ACS Catal.* **2024**, *14* (7), 5326−5343.
(16) Shiraishi, Y.; Ueda, Y.; Soramoto, A.; Hinokuma, S.; Hirai, T. Photocatalytic Hydrogen Peroxide Splitting on Metal-Free Powders Assisted by Phosphoric Acid as a Stabilizer. *Nat. Commun.* **2020**, *11*, No. 3386.
(17) Lee, J.; Lee, S. M.; Chen, S.; Kumari, T.; Kang, S.; Cho, Y.; Yang, C. Organic Photovoltaics with Multiple Donor-Acceptor Pairs. *Adv. Mater.* **2019**, *31* (20), No. 1804762.
(18) Chang, J.; Zhang, G.; Zhang, C.; Xu, C.; Xia, H.; Deng, W.; Zhao, X. Characterizing the Thickness Distribution of Donor and Acceptor in Organic Photovoltaics via Quasi-Monochromatic Light Transmittance. *Adv. Opt. Mater.* **2024**, *12* (13), No. 2302693.
(19) Liu, Z.; Zhang, J.; Wan, Y.; Chen, J.; Zhou, Y.; Zhang, J.; Wang, G.; Wang, R. Donor-Acceptor Structural Polymeric Carbon Nitride with In-Plane Electric Field Accelerating Charge Separation for Efficient Photocatalytic Hydrogen Evolution. *Chem. Eng. J.* **2022**, *430*, No. 132725.
(20) Che, H.; Wang, J.; Wang, P.; Ao, Y.; Chen, J.; Gao, X.; Zhu, F.; Liu, B. Simultaneously Achieving Fast Intramolecular Charge Transfer and Mass Transport in Holey D-π-A Organic Conjugated Polymers for Highly Efficient Photocatalytic Pollutant Degradation. *JACS Au* **2023**, *3* (5), 1424−1434.
(21) Zhang, G.; Lin, L.; Li, G.; Zhang, Y.; Savateev, A.; Zafeiratos, S.; Wang, X.; Antonietti, M. Ionothermal Synthesis of Triazine-Heptazine-Based Copolymers with Apparent Quantum Yields of 60% at 420 nm for Solar Hydrogen Production from "Sea Water". *Angew. Chem., Int. Ed.* **2018**, *57*, 9372−9376.
(22) Li, C.; Wu, H.; Du, Y.; Xi, S.; Dong, H.; Wang, S.; Wang, Y. Mesoporous 3D/2D NiCoP/g-C_3N_4 Heterostructure with Dual Co-N and Ni-N Bonding States for Boosting Photocatalytic H_2 Production Activity and Stability. *ACS Sustainable Chem. Eng.* **2020**, *8* (34), 12934−12943.
(23) Yu, Y.; Yan, W.; Wang, X.; Li, P.; Gao, W.; Zou, H.; Wu, S.; Ding, K. Surface Engineering for Extremely Enhanced Charge Separation and Photocatalytic Hydrogen Evolution on g-C_3N_4. *Adv. Mater.* **2018**, *30* (9), No. 1705060.
(24) Ho, W.; Zhang, Z.; Lin, W.; Huang, S.; Zhang, X.; Wang, X.; Huang, Y. Copolymerization with 2,4,6-Triaminopyrimidine for the Rolling-up the Layer Structure, Tunable Electronic Properties, and Photocatalysis of g-C_3N_4. *ACS Appl. Mater. Interfaces* **2015**, *7* (9), 5497−5505.
(25) Qin, Y.; Lu, J.; Meng, F.; Lin, X.; Feng, Y.; Yan, Y.; Meng, M. Rationally Constructing of a Novel 2D/2D WO_3/Pt/g-C_3N_4 Schottky-Ohmic Junction towards Efficient Visible-Light-Driven Photocatalytic Hydrogen Evolution and Mechanism Insight. *J. Colloid Interface Sci.* **2021**, *586*, 576−587.
(26) Zhu, Z.; Xing, X.; Qi, Q.; Li, H.; Han, D.; Song, X.; Tang, X.; Ng, H.; Huo, P. Regulation CN Reduction of CO_2 Products Selectivity by Adjusting the Number of V Sites and Mechanism Exploration. *Fuel* **2025**, *288*, No. 134509.
(27) Xu, C.; Liu, X.; Li, D.; Chen, Z.; Yang, J.; Huang, J.; Pan, H. Coordination of π-Delocalization in g-C_3N_4 for Efficient Photocatalytic Hydrogen Evolution under Visible Light. *ACS Appl. Mater. Interfaces* **2021**, *13* (17), 20114−20124.
(28) Zhou, L.; Pan, L.; Kong, W.; Zhou, S.; Yang, F.; Gao, S.; Kong, Y. Coupling In-plane π-Electrons with Oxygen-Heteroatom in Ultrathin g-C_3N_4 Nanosheets for Markedly Improved Photodegradation Activity. *ACS Appl. Opt. Mater.* **2023**, *1* (1), 216−228.
(29) Liu, J.; Yu, Y.; Qi, R.; Cao, C.; Liu, X.; Zheng, Y.; Song, W. Enhanced Electron Separation on In-Plane Benzene-Ring Doped g-C_3N_4 Nanosheets for Visible Light Photocatalytic Hydrogen Evolution. *Appl. Catal., B* **2019**, *244*, 459−464.
(30) Wang, T.; Li, M.; Chen, Y.; Che, X.; Bi, F.; Yang, Y.; Yang, R.; Li, C. Regioisomeric Benzotriazole-Based Covalent Organic Frameworks for High Photocatalytic Activity. *ACS Catal.* **2023**, *13* (23), 15439−15447.
(31) Qin, Y.; Li, H.; Lu, J.; Meng, F.; Ma, C.; Yan, Y.; Meng, M. Nitrogen-Doped Hydrogenated TiO_2 Modified with CdS Nanorods with Enhanced Optical Absorption, Charge Separation and Photocatalytic Hydrogen Evolution. *Chem. Eng. J.* **2020**, *384*, No. 123275.
(32) Yang, X.; Lu, Y.; Sun, Z.; Cui, K.; Tan, Z. Measurement and Correlation of Phase Equilibria in Aqueous Two-Phase Systems Containing Polyoxyethylene Cetyl Ether and Three Organic Salts at Different Temperatures. *J. Chem. Eng. Data* **2018**, *63*, 625−634.
(33) Qin, Y.; Wang, Y.; Lu, J.; Xu, L.; Wong, W.-Y. A Highly Conjugated Nickel(II)-Acetylide Framework for Efficient Photocatalytic Carbon Dioxide Reduction. *Angew. Chem., Int. Ed.* **2025**, *64*, No. e202418269.
(34) Lu, Y.; Cong, B.; Tan, Z.; Yan, Y. Synchronized Separation, Concentration and Determination of Trace Sulfadiazine and Sulfamethazine in Food and Environment by Using Polyoxyethylene Lauryl Ether-Salt Aqueous Two-Phase System Coupled to High-Performance Liquid Chromatography. *Ecotoxical. Environ. Safe.* **2016**, *133*, 105−113.
(35) Ruan, X.; Huang, C.; Cheng, H.; Zhang, Z.; Cui, Y.; Li, Z.; Xie, T.; Ba, K.; Zhang, H.; Zhang, L.; Zhao, X.; Leng, J.; Jin, S.; Zhang, W.; Zheng, W.; Ravi, S. K.; Jiang, Z.; Cui, X.; Yu, J. A Twin S-Scheme Artificial Photosynthetic System with Self-Assembled Heterojunctions Yields Superior Photocatalytic Hydrogen Evolution Rate. *Adv. Mater.* **2023**, *35* (6), No. 2209141.
(36) Zheng, Y.; Cui, Y.; Ruan, Q.; Zhao, Y.; Hou, H.; Zhou, Y.; Ling, C.; Wang, J.; Chen, Z.; Guo, X. Heavily Doped Carbon Nitride Nanocrystal Promotes Visible-Near-Infrared Photosynthesis of Hydrogen Peroxide with Near-Unit Photon Utilization. *ACS Nano* **2024**, *18* (22), 14583−14594.
(37) Qin, Y.; Lu, J.; Zhang, C.; Xu, L.; Wong, W.-Y. Auxiliary Ligand-Coordinated Nanoconfined Hydrophobic Microenvironments in Nickel(II)−Acetylide Framework for Enhanced CO_2 Photoreduction. *Angew. Chem., Int. Ed.* **2025**, *64*, No. e202505883.
(38) Zhu, X.; Xu, H.; Liu, J.; Bi, C.; Tian, J.; Zhong, K.; Wang, B.; Ding, P.; Wang, X.; Chu, P. K.; Xu, H.; Ding, J. Stacking Engineering of Heterojunctions in Half-Metallic Carbon Nitride for Efficient CO_2 Photoreduction. *Adv. Sci.* **2023**, *10* (36), No. 2307192.
(39) Zhu, Z.; Shen, W.; Li, D.; Ye, J.; Song, X.; Tang, X.; Zhao, J.; Huo, P. Oxygen-Doped Red Carbon Nitride: Enhanced Charge Separation and Light Absorption for Robust CO_2 Photoreduction. *Inorg. Chem.* **2023**, *62*, 15432−15439.

https://doi.org/10.1021/acscatal.5c06958
ACS Catal. 2026, 16, 4440−4448